MIMO Coded Generalized Reduced Dimension Fourier Algorithm for 3D Microwave Imaging

Amir Masoud Molaei, Shaoqing Hu, *Member, IEEE*, Rupesh Kumar, and Okan Yurduseven, *Senior Member, IEEE*

Abstract—In this paper, to accelerate data acquisition and image reconstruction procedures in a multistatic short-range microwave imaging scenario, an orthogonal coding approach with Fourier domain processing is presented. First, a special two-dimensional (2D) multiple-input multiple-output (MIMO) structure is introduced to fully electronically synthesize the 2D aperture. Then, the model of the transmitted and received signals by a MIMO stepped-frequency-modulated radar is presented, with special considerations about orthogonal, balanced and optimal sequences. On the receiver side, the backscatter frequency response extraction process is formulated with the aim of obtaining individual information of all channels. Finally, based on the introduced model, a fast Fourier-based algorithm with reduced dimensions, named MIMO coded generalized reduced dimension Fourier (CGRDF), is mathematically derived. It includes extracting phase and amplitude compensators with the aim of mapping 4D to 2D spatial data, transferring the backscatter transfer function from the spatial domain to the wavenumber domain, extracting the smoothing filter, compensating the curvature of the wavefront of all scatterers, extracting the reflectivity function and an additional range compensator. The results of numerical simulations show the satisfactory and reliable performance of the proposed approach in terms of the information retrieval process and processing speed.

Index Terms—Coded generalized RDF, MIMO, short-range, 3D microwave imaging.

I. INTRODUCTION

DUE to a wide range of applications of microwave radar imaging in medical diagnosis, nondestructive testing and evaluation, security screening, structural health monitoring and through-wall imaging, this field has seen significant progress in physical, system and processing layers in recent years [1-3].

To reconstruct a three-dimensional (3D) image of a scene/target, a 2D aperture must be synthesized. This usually

Amir Masoud Molaei, Rupesh Kumar and Okan Yurduseven are with the Institute of Electronics, Communications, and Information Technology, Queen's University Belfast, Belfast BT3 9DT, U.K. (e-mails: a.molaei@qub.ac.uk; r.kumar@qub.ac.uk; okan.yurduseven@qub.ac.uk).

Shaoqing Hu is with the College of Engineering, Design and Physical Sciences, Brunel University London, Uxbridge UB8 3PH, U.K. (e-mail: shaoqing.hu@brunel.ac.uk).

Color versions of one or more of the figures in this article are available online at http://ieeexplore.ieee.org

requires a very large number of antenna elements to satisfy the Nyquist criterion [4]. The use of sparse aperiodic phased arrays [5, 6] and multistatic multiple-input multiple-output (MIMO) arrays [7, 8] are two solutions provided for this issue. It has been demonstrated that the high spatial information diversity obtained by antenna arrays with a MIMO configuration can lead to an increase in the quality of reconstructed images in an imaging system [9, 10]. Another major advantage of a MIMO array compared to a phased array is that a MIMO array has the potential to apply different antenna elements and/or waveforms to achieve simultaneous transmission and reception [11]. The importance of simultaneous transmission by transmitters (Txs) is the drastic reduction of data acquisition time. However, this requires that the processor on the receiver (Rx) side is somehow able to identify/separate the information of each pair of individual Tx-Rx channels. Using orthogonal signals/information is a suitable way to achieve this purpose [12, 13]. Recently, in [14, 15], coding-based mechanisms have been developed for radar imaging by frequency-modulated (FM) continuous-wave radar. Although these mechanisms minimize the required bandwidth and sampling rate, they have considerable complexity both on the Tx and Rx sides. Pedross-Engel et al. [16] presented a reliable approach that uses orthogonal coded signals for scene illumination. However, the image reconstruction process in [16] is based on a computationally complex least-squares (LS) technique, which limits its real-time application.

Fourier-based image reconstruction techniques [17-19] are computationally efficient alternatives to methods such as LS and matched filter [20]. The range migration algorithm (RMA) is a conventional technique for image reconstruction in the Fourier domain [21, 22]. Its generalized versions for the MIMO scenario [10, 23] are very efficient compared to non-Fourier techniques; however, they still include 4D Fourier transforms and a Stolt interpolation (generally 5D to 3D in the wavenumber domain) [10, 13]. Recently, in [24], an algorithm called reduced dimension Fourier (RDF) has been presented to reduce the dimensions of Fourier operations. However, it has only been developed for 1D arrays, specifically sparse periodic arrays, and with the assumption of mechanical scanning perpendicular to the array, which requires significant data acquisition time. For real-time applications, sliding imaging systems with mechanical scanning are challenging.

To overcome the challenges of data acquisition and the complexity of the image reconstruction algorithms mentioned above, in this paper, we first introduce a special 2D MIMO structure to fully electronically synthesize the 2D aperture. We

will prove that under a short-range (in the near-field (NF) region) [25, 26] multistatic imaging scenario, such a special structure can reliably lead us in reducing the dimensionality of raw spatial data from 4D to 2D ready for fast Fourier calculations. Then, the mathematical model of transmission and reception by a MIMO stepped-FM radar is expressed, taking into account special considerations about code sequences and the process of extracting the transfer function. Finally, based on the introduced model for the system and data, a fast Fourier-based algorithm with reduced dimensions (both in Fourier calculations and in the interpolation procedure) named MIMO coded generalized RDF (CGRDF) is derived. This part includes derivations of phase and amplitude compensators with the aim of mapping spatial data from 4D to 2D, transferring the backscatter frequency response from the spatial domain to the wavenumber domain, extracting the smoothing filter, compensating the wavefront curvature of all scatterers (Stolt interpolation), extracting the spatial reflectivity function and an additional range compensator to mitigate the effect of propagation loss in the reconstructed image. It will be shown how the proposed algorithm settles for a 3D-to-3D interpolation by eliminating the 5D-to-3D interpolation that is required to resample the data onto a quasi-uniform grid of the wavenumbers. This can be very effective in reducing the volume of calculations. In the mathematical derivation of the above algorithm, both terms of phases and amplitudes are taken into account, which leads to the production of more accurate final results. The performance of the proposed approach is qualitatively and quantitatively evaluated and discussed in various aspects by numerical simulations.

In summary, the main novelties and contributions of this work are listed below:

- Introduction of a special 2D MIMO structure to fully electronically synthesize the 2D aperture, for a NF multistatic imaging scenario, to reduce the dimensionality of spatial raw data without losing valuable information and be compatible with fast Fourier-based calculations.

- Introducing an efficient model based on orthogonal coding with the aim of transmitting simultaneously by all Txs and with the ability to extract channels information separately. In addition, before using the codes, they are improved in terms of temporal correlation properties by defining an optimization problem and solving it.

- Mathematical development of the RDF image reconstruction algorithm to a more general mode (fully electronic scanning scenario). The proposed MIMO CGRDF algorithm has the following unique features:

  ❖ Contrary to common works, both terms of phases and amplitudes are fully taken into account in the derivation.

  ❖ By benefiting from the introduced structure, the base of calculations with smaller dimensions, and as a result, less complexity is provided.

  ❖ Alleviation of the common propagation loss effect in reconstructed images.

The rest of this paper is organized as follows: In Section II, first, the specific model of the system and data is introduced; then special considerations related to orthogonal code sequences in the proposed approach and also how to extract the channel transfer function are presented; finally, the proposed image reconstruction algorithm is derived mathematically. In Section III, the performance of the proposed approach is evaluated and discussed from various aspects through several experiments. Section IV is devoted to conclusions. Also, the details of some mathematical calculations and derivations are given in the appendix section.

Notation: Throughout the paper, superscripts $(.)^H$ and $(.)^T$ represent the conjugate transpose and transpose, respectively. The symbols j, $\mathbf{I}_m$, $\mathbf{0}_m$, $\mathbf{1}_m$, $\min_x$, $\max_x$, $\mathrm{Re}\{.\}$, $\mathbb{E}\{.\}$ and $\mathcal{O}(.)$ denote the imaginary unit, $m \times m$ identity and zero matrices, $m \times 1$ vector with all entries equal to one, minimum and maximum values with decision variable x, real part, expected value operator, and asymptotic order of computational complexity, respectively.

II. PROPOSED APPROACH

First, in Section II-A, the system and data model in the proposed approach are introduced. Then, in Section II-B, special considerations regarding the selection of code sequences on the Tx side and the procedure of extracting the transfer function on the Rx side are presented. Finally, in Section II-C, based on the introduced model, the proposed algorithm for image reconstruction is described.

A. System and Data Model

In the proposed approach, it is assumed that radar measurements are obtained fully electronically by two uniform rectangular arrays (URAs), as Tx and Rx, in the multistatic MIMO structure shown in Fig. 1(a). The physical Tx and Rx URAs are composed of $N_{T_x} \times N_{T_y}$ and $N_{R_x} \times N_{R_y}$ antenna elements, respectively, with inter-element spacings of d_{T_x} and d_{R_x} along the x-axis (horizontal), and d_{T_y} and d_{R_y} along the y-axis (vertical). To create a uniform effective aperture consisting of virtual elements with uniform inter-element spacing (see Fig. 1(b)), there must be a specific relationship between the number of physical antennas and the spacing between them. Creating a uniform synthesized aperture will provide the necessary conditions for the development of the algorithm proposed in Section II-C based on fast Fourier calculations. According to the effective phase center principle [27], under the far-field (FF) assumption, it can be easily proved that if $d_{T_x} = N_{R_x} d_{R_x}$ and $d_{T_y} = N_{R_y} d_{R_y}$ are chosen, then the resulting effective aperture is a monostatic virtual URA with a size of $N_x \times N_y$ and inter-element spacings of $d_x = d_{R_x}/2$ and $d_y = d_{R_y}/2$, respectively, in the horizontal and vertical directions, where $N_x = N_{T_x} N_{R_x}$ and $N_y = N_{T_y} N_{R_y}$.

(a)

(b)
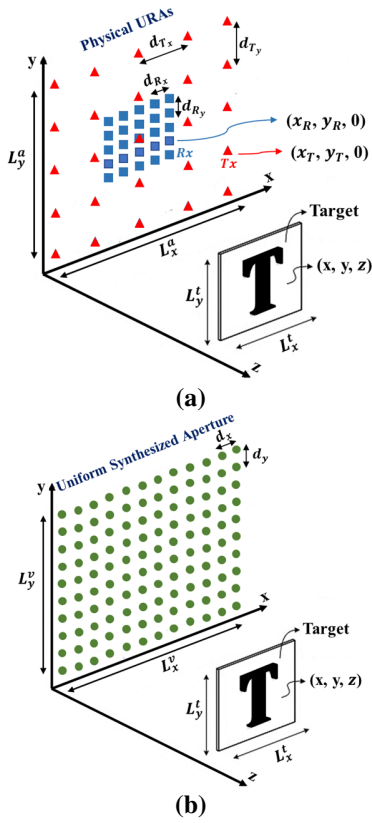
Fig. 1. The general structure of MIMO transceiver arrays in the proposed approach; (a) multistatic physical arrays, (b) equivalent monostatic virtual array under the FF assumption.

Remark 1: Note that it has been demonstrated that the inter-element spacing in the Tx array can take values larger than half wavelength without suffering from ambiguity at the receiving end [28, 29].

To illuminate the scene, a stepped-FM MIMO radar [16, 30] is considered. The i-th Tx antenna emits a binary phase-shift keying (BPSK) modulated signal, considering the i-th column of the matrix of binary code symbols (i.e. $\mathbf{\Phi}_{L \times N_T} \triangleq \left[\mathbf{\varphi}_1, \mathbf{\varphi}_2, ..., \mathbf{\varphi}_{N_T} \right]$), which satisfies the mutual orthogonality condition in (2), in the following form:

$$x_i(t) = \text{Re}\left\{ \sum_{l=1}^{L} \varphi_{l,i} P_T(t - lT) e^{j2\pi ft} \right\} \quad (1)$$

$$\mathbf{\Phi}^H \mathbf{\Phi} = L\mathbf{I}_{N_T}, \quad (2)$$

where L, f, and P_T respectively represent the code length, carrier frequency, and unit rectangular pulse function with duration T, and $\mathbf{\varphi}_i \triangleq \left[\varphi_{1,i}, \varphi_{2,i}, ..., \varphi_{L,i} \right]^T$, $\varphi_{l,i} \in \{-1,+1\}$, $N_T = N_{T_x} N_{T_y}$, $i = 1, 2, ..., N_T$ and $N_T < L$. In fact, in (1), the BPSK modulator modulates a sequence of constant amplitude tones with a phase shift of 0 or π radians, which is controlled

by the code symbol sequence. The signal received by the i'-th element of the Rx array can be modeled as follows:

$$s_{i'}(t) = \sum_{i=1}^{N_T} \text{Re}\left\{ H_{i,i'}(f) \sum_{l=1}^{L} \varphi_{l,i} P_T(t - lT) e^{j2\pi ft} \right\} + n_{i'}(t), \quad (3)$$

where $n_{i'}(t)$ is the measurement noise, and $N_R = N_{R_x} N_{R_y}$ and $i' = 1, 2, ..., N_R$. In (3), $H_{i,i'}(f)$ denotes the backscatter frequency response corresponding to the i-th Tx antenna and the i'-th Rx antenna at frequency f. Assuming that the scene consists of $N'_x \times N'_y \times N'_z$ hypothesized point scatterers with reflectivities $\{\rho_p\}$, where $p = 1, 2, ..., N'_x \times N'_y \times N'_z$, we have [31]

$$H_{i,i'}(f) = \sum_{p=1}^{N'_x \times N'_y \times N'_z} \rho_p \chi_{i,i',p} e^{-j2\pi f \tau_{i,i',p}}, \quad (4)$$

where $\chi_{i,i',p}$ and $\tau_{i,i',p}$ respectively represent the round-trip path loss and round-trip propagation delay of the electromagnetic wave in free space corresponding to the i-th Tx, i'-th Rx and p-th point scatterer.

After down-conversion and sampling with a sampling period T [16], the sampled received signal $s_{i'}[l] = s_{i'}(lT)$ can be expressed in the following form:

$$s_{i'}[l] = \sum_{i=1}^{N_T} H_{i,i'}(f) \varphi_{l,i} + d_{i'} + n_{i'}[l], \quad (5)$$

where $d_{i'}$ represents the direct current (DC) offset introduced by non-ideal down-converters [32].

B. Special Considerations Regarding Code Sequences and Transfer Function Extraction Procedure

1) Special considerations about code sequences on the Tx side: A matrix $\mathbf{W}_{L \times L}$ with entries ± 1 (L can be 1, 2 or a multiple of 4), whose distinct column (or row) vectors are orthogonal, is known as a Hadamard matrix of order L [33]. It is clear that the column sequences of such a matrix can provide the condition required in (2). However, the original sequences of Hadamard codes suffer from poor auto-correlation properties due to their very regular structure [34]. In other words, mathematically, the auto-correlation functions (ACFs) of the original Hadamard matrix code sequences have high peak values even when the delay time is non-zero. This problem may cause the system performance to drop excessively in any possible timing mismatch conditions [35]. Therefore, in this subsection, we modify the structure of the Hadamard matrix in such a way that in addition to maintaining the orthogonality condition, the temporal correlation properties of the original structure are improved under the mentioned conditions.

Aperiodic ACF of φ_i is defined as follows [36]:

$$A_i(l) = \begin{cases} \dfrac{1}{L}\sum_{k=0}^{L-l-1}\varphi_{k,i}\varphi_{k+l,i}^*, & 0 \le l \le L-1, \\ \dfrac{1}{L}\sum_{k=0}^{L+l-1}\varphi_{k-l,i}\varphi_{k,i}^*, & 1-L \le l < 0, \\ 0, & |l| \ge L. \end{cases} \quad (6)$$

The goal is that the maximum values of out-of-phase aperiodic ACFs are as small as possible. Therefore, we define a fitness function with integer constraints in the following form:

$$\min_{\mathbf{x}} f(\mathbf{x}) \text{ such that } \begin{cases} 1 \le x_k \le L, \\ L - L_u \le 0, \\ \mathbf{x} = [x_1, x_2, ..., x_L] \in \mathbb{Z}, \end{cases} \quad (7)$$

$$f(\mathbf{x}) \triangleq \sum_{l=1-L}^{L-1} \max_m \left| \tilde{A}_m(l) \right|, \quad m = 2, 3, ..., N_T + 1,$$

where L_u represents the length of the unique values in the vector $\mathbf{x}$, $\tilde{A}_m(l)$ denotes the aperiodic ACF of $\tilde{\varphi}_m$ belonging to the matrix $\tilde{\mathbf{\Phi}}_{L \times N_T} \triangleq \mathbf{\Phi}(\mathbf{x}, 2 : N_T + 1)$, and $N_T < L$. Since the above optimization problem has integer nonlinear constraints, genetic algorithms (GAs), surrogate optimization, etc. can be used to solve it [37-39]. It has been demonstrated that GA solves the integer problems best when lower and upper bounds are provided for every component of $\mathbf{x}$ [40]. For this reason, we have used it for the optimization process in Section III.

Another issue that we consider in practice at the stage of choosing code sequences is that, in addition to orthogonality, the sequences should be completely balanced (the number of positive and negative unity bits should be equal); that is, mathematically, $\mathbf{\Phi}^H \mathbf{1}_L = \mathbf{0}_{N_T}$. This makes their decoding by processors to be done efficiently [41]. Fortunately, the columns of the Hadamard matrix with any order (except the first column) have such a property. Therefore, it is enough to ignore its first column. That is why in (7) the values of m, which correspond to the index of sequences related to Txs, are defined between 2 and $N_T + 1$, and $N_T < L$.

Therefore, finally, what is considered as the matrix of binary code symbols $\mathbf{\Phi}$ is $\tilde{\mathbf{W}}_{L \times N_T} \triangleq \mathbf{W}(\mathbf{x}, 2 : N_T + 1)$. Note that in this case, the orthogonality and balance of the sequences are still preserved because the order of the bits in all the sequences is shifted identically, so $\tilde{\mathbf{W}}^T \tilde{\mathbf{W}} = L\mathbf{I}_{N_T}$ and $\tilde{\mathbf{W}}^T \mathbf{1}_L = \mathbf{0}_{N_T}$.

2) Channel transfer function extraction: By collecting and concatenating L samples received from the i'-th Rx at frequency f, and according to the explanation of subsection II-B-1, (5) can be written in matrix form as follows:

$$\mathbf{s}_{i'} = \tilde{\mathbf{W}}\mathbf{H}_{i'}(f) + d_{i'}\mathbf{1}_L + \mathbf{n}_{i'}, \quad (8)$$

where

$$\mathbf{s}_{i'} = \left[s_{i'}[1], s_{i'}[2], ..., s_{i'}[L] \right]^T \in \mathbb{C}^{L \times 1},$$

$$\mathbf{H}_{i'}(f) = \left[H_{1,i'}(f), H_{2,i'}(f), ..., H_{N_T,i'}(f) \right]^T \in \mathbb{C}^{N_T \times 1}, \quad (9)$$

$$\mathbf{n}_{i'} = \left[n_{i'}[1], n_{i'}[2], ..., n_{i'}[L] \right]^T \in \mathbb{C}^{L \times 1}.$$

Due to the orthogonality property in the matrix $\tilde{\mathbf{W}}$, an estimate of the channel transfer function can be obtained from (8) in the following form:

$$\hat{\mathbf{H}}_{i'}(f) = \frac{1}{L}\tilde{\mathbf{W}}^T \mathbf{s}_{i'}. \quad (10)$$

Note that according to the balanced property in $\tilde{\mathbf{W}}$, $\tilde{\mathbf{W}}^T \mathbf{1}_L = \mathbf{0}_{N_T}$. Therefore, the effect of DC offset in (10) is neutralized.

C. Image Reconstruction

The 3D reconstruction of the scene image means obtaining an estimate of the spatial reflectivity function $\rho(x, y, z)$, which affects the backscatter frequency response (channel transfer function) according to (4). According to the geometry of the system in Fig. 1(a), the backscatter frequency response can be written as a spatial-frequency expression in the following form [13, 42]:

$$H\left(x_{T_i}, x_{R_{i'}}, y_{T_i}, y_{R_{i'}}; f\right) = \int_V \frac{\rho(x, y, z)}{16\pi^2 D_{T_i} D_{R_{i'}}} e^{-jk\left(D_{T_i} + D_{R_{i'}}\right)} dV, \quad (11)$$

where $k = 2\pi f / c$ represents the wavenumber, c is the speed of light, $dV = dxdydz$ and

$$D_{T_i} = \sqrt{\left(x - x_{T_i}\right)^2 + \left(y - y_{T_i}\right)^2 + z^2}, \quad (12)$$

$$D_{R_{i'}} = \sqrt{\left(x - x_{R_{i'}}\right)^2 + \left(y - y_{R_{i'}}\right)^2 + z^2}. \quad (13)$$

According to (11), the backscatter frequency response in the current form is a 5D data. Therefore, extracting the reflectivity function with Fourier-based techniques directly from it requires multi-dimensional and complex calculations (taking the 4D Fourier transform (FT) and interpolating the 5D to 3D) [3, 13]. In order to significantly reduce the amount of computation, we map the 5D data $\hat{H}\left(x_{T_i}, x_{R_{i'}}, y_{T_i}, y_{R_{i'}}; f\right)$ to a

3D data $\tilde{H}\left(x_{C_{i'}}, y_{C_{i'}}; f\right)$, so that $\left(x_{C_{i'}}, y_{C_{i'}}, 0\right)$ represents the coordinates of the virtual elements shown in the grid of Fig. 1(b), where $i'' = 1, 2, ..., N_T N_R$. Since in this paper, we are dealing with a NF multistatic imaging scenario, to match the uniform grid shown in Fig. 1(b), it is necessary to derive phase and amplitude compensations to apply to the raw data $\hat{H}$. Specifically, the reason for this is that under a FF scenario, we can assume D_{T_i} and $D_{R_{i'}}$ as well as their corresponding distance in the virtual grid (i.e. $D_{C_{i'}}$) to be approximately equal to each other (see Fig. 2), but this is not acceptable under the NF scenario. The range of the NF region depends on the wavelength λ and the array aperture length L_{ape} and is defined as $\left[0.62\sqrt{L_{ape}^3/\lambda}, 2L_{ape}^2/\lambda\right]$ [43].
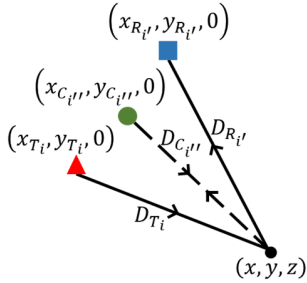
Fig. 2. The coordinates and distances of the physical Tx and Rx antennas and the corresponding virtual element to a point scatterer.

Suppose that the coordinates of the physical antennas in $\left(x_{T_i}, y_{T_i}, 0\right)$ and $\left(x_{R_{i'}}, y_{R_{i'}}, 0\right)$ have a shift of $\alpha_{i''}$ in the horizontal direction and a shift of $\beta_{i''}$ in the vertical direction compared to the coordinates of the corresponding virtual element in their center (i.e. $\left(x_{C_{i'}}, y_{C_{i'}}, 0\right)$); that is,

$$
\begin{aligned}
x_{T_i} &= x_{C_{i'}} - \alpha_{i''}, \\
y_{T_i} &= y_{C_{i'}} - \beta_{i''},
\end{aligned}
\tag{14}
$$

$$
\begin{aligned}
x_{R_{i'}} &= x_{C_{i'}} + \alpha_{i''}, \\
y_{R_{i'}} &= y_{C_{i'}} + \beta_{i''}.
\end{aligned}
\tag{15}
$$

Clearly, the value of $D_{C_{i'}}$ can be calculated as follows (see Fig. 2):

$$
D_{C_{i'}} = \sqrt{\left(x - x_{C_{i'}}\right)^2 + \left(y - y_{C_{i'}}\right)^2 + z^2}.
\tag{16}
$$

According to (12) and (14), as well as (13) and (15), $D_{C_{i'}}$ can be rewritten in terms of D_{T_i} and $D_{R_{i'}}$ as (17) and (18), respectively

$$
D_{C_{i'}} = \sqrt{D_{T_i}^2 - 2\alpha_{i''}\left(x - x_{T_i}\right) - 2\beta_{i''}\left(y - y_{T_i}\right) + \alpha_{i''}^2 + \beta_{i''}^2}.
\tag{17}
$$

$$
D_{C_{i'}} = \sqrt{D_{R_{i'}}^2 + 2\alpha_{i''}\left(x - x_{R_{i'}}\right) + 2\beta_{i''}\left(y - y_{R_{i'}}\right) + \alpha_{i''}^2 + \beta_{i''}^2}.
\tag{18}
$$

Total round-trip distance in virtual elements can be considered as the sum of the expressions on the right sides of (17) and (18)

$$
\begin{aligned}
\tilde{D}_{C_{i'}} &\triangleq 2D_{C_{i'}} \\
&= \sqrt{D_{T_i}^2 - 2\alpha_{i''}\left(x - x_{T_i}\right) - 2\beta_{i''}\left(y - y_{T_i}\right) + \alpha_{i''}^2 + \beta_{i''}^2} \\
&\quad + \sqrt{D_{R_{i'}}^2 + 2\alpha_{i''}\left(x - x_{R_{i'}}\right) + 2\beta_{i''}\left(y - y_{R_{i'}}\right) + \alpha_{i''}^2 + \beta_{i''}^2}.
\end{aligned}
\tag{19}
$$

By applying 2D Taylor series expansion [44] with respect to $\alpha_{i''}$ and $\beta_{i''}$ around zero, an approximation of $\tilde{D}_{C_{i'}}$ is provided as (20). By ignoring the terms of the distance with powers of three in the denominator, we have

---

$$
\begin{aligned}
\tilde{D}_{C_{i'}} &\simeq D_{T_i} + D_{R_{i'}} - \frac{\alpha_{i''}\left(x - x_{T_i}\right)}{D_{T_i}} + \frac{\alpha_{i''}\left(x - x_{R_{i'}}\right)}{D_{R_{i'}}} - \frac{\beta_{i''}\left(y - y_{T_i}\right)}{D_{T_i}} + \frac{\beta_{i''}\left(y - y_{R_{i'}}\right)}{D_{R_{i'}}} \\
&\quad + \frac{1}{2}\left[\alpha_{i''}^2\left(\frac{1}{D_{T_i}} + \frac{1}{D_{R_{i'}}} - \frac{\left(x - x_{T_i}\right)^2}{D_{T_i}^3} - \frac{\left(x - x_{R_{i'}}\right)^2}{D_{R_{i'}}^3}\right) + \beta_{i''}^2\left(\frac{1}{D_{T_i}} + \frac{1}{D_{R_{i'}}} - \frac{\left(y - y_{T_i}\right)^2}{D_{T_i}^3} - \frac{\left(y - y_{R_{i'}}\right)^2}{D_{R_{i'}}^3}\right) \\
&\quad - 2\alpha_{i''}\beta_{i''}\left(\frac{\left(x - x_{T_i}\right)\left(y - y_{T_i}\right)}{D_{T_i}^3} - \frac{\left(x - x_{R_{i'}}\right)\left(y - y_{R_{i'}}\right)}{D_{R_{i'}}^3}\right)\right].
\end{aligned}
\tag{20}
$$

$$\tilde{D}_{C_{i'}} \simeq D_{T_i} + D_{R_{i'}}$$

$$+ \frac{-\alpha_{i'}\left(x-x_{T_i}\right)-\beta_{i'}\left(y-y_{T_i}\right)+\dfrac{\alpha_{i'}^2+\beta_{i'}^2}{2}}{D_{T_i}} \qquad (21)$$

$$+ \frac{\alpha_{i'}\left(x-x_{R_{i'}}\right)+\beta_{i'}\left(y-y_{R_{i'}}\right)+\dfrac{\alpha_{i'}^2+\beta_{i'}^2}{2}}{D_{R_{i'}}}.$$

Finally, by considering $\left(x-x_{T_i}\right)^2, \left(y-y_{T_i}\right)^2, \left(x-x_{R_{i'}}\right)^2, \left(y-y_{R_{i'}}\right)^2 \ll z^2$ and $z \simeq z_0$, where z_0 represents the range in the center of the scene, and according to (14) and (15), an approximation of the total round-trip distance for phase compensation in virtual elements can be calculated as follows:

$$\tilde{D}_{C_{i'}} \simeq D_{T_i} + D_{R_{i'}} - \frac{\alpha_{i'}^2+\beta_{i'}^2}{z_0}. \qquad (22)$$

On the other hand, with the aim of compensating the amplitude, the total round-trip path loss in virtual elements can be considered as the multiplication of the expressions on the right of (17) and (18)

$$\breve{D}_{C_{i'}} \triangleq D_{C_{i'}}^2$$

$$= \sqrt{D_{T_i}^2 - 2\alpha_{i'}\left(x-x_{T_i}\right)-2\beta_{i'}\left(y-y_{T_i}\right)+\alpha_{i'}^2+\beta_{i'}^2} \qquad (23)$$

$$\sqrt{D_{R_{i'}}^2 + 2\alpha_{i'}\left(x-x_{R_{i'}}\right)+2\beta_{i'}\left(y-y_{R_{i'}}\right)+\alpha_{i'}^2+\beta_{i'}^2}.$$

By calculating the terms of the Taylor series expansion, this time for $\breve{D}_{C_{i'}}$ and after some mathematical simplifications, we have (24). With a method like the previous paragraph and ignoring the terms of the distance with powers of four in the denominator, we have

$$\breve{D}_{C_{i'}} \simeq D_{T_i} D_{R_{i'}} \left[\frac{z_0^2 - \left(\alpha_{i'}^2+\beta_{i'}^2\right)}{z_0^2} \right]. \qquad (25)$$

In (22) and (25), $\alpha_{i'}$ and $\beta_{i'}$ can be calculated as $x_{C_{i'}} - x_{T_i}$ and $y_{C_{i'}} - y_{T_i}$ (or equivalently $x_{R_i} - x_{C_{i'}}$ and $y_{R_i} - y_{C_{i'}}$) respectively. In the approximations used in (21) and (25), in order to simplify long expressions and also to achieve approximate terms independent of the target positions (except the range in the center of the scene), terms containing distances in the denominator with higher powers have been ignored compared to lower exponents. These simplifications are reasonable because D_{T_i} and $D_{R_{i'}}$ are dependent on the target range and are dominant in terms of amplitude.

Now, by using approximations $\tilde{D}_{C_{i'}}$ and $\breve{D}_{C_{i'}}$ in (22) and (25), respectively, the reduced dimension data of $\tilde{H}\left(x_{C_{i'}}, y_{C_{i'}}; f\right)$ can be written in the following form:

$$\tilde{H}\left(x_{C_{i'}}, y_{C_{i'}}; f\right) \simeq$$
$$\frac{z_0^2}{z_0^2 - \left(\alpha_{i'}^2+\beta_{i'}^2\right)} \hat{H}\left(x_{T_i}, x_{R_{i'}}, y_{T_i}, y_{R_{i'}}; f\right) e^{jk\frac{\alpha_{i'}^2+\beta_{i'}^2}{z_0}}. \qquad (26)$$

Therefore, according to (19), (23) and (26), (11) is simplified to the following form:

$$\tilde{H}\left(x_{C_{i'}}, y_{C_{i'}}; f\right) \simeq$$

$$\frac{z_0^2}{z_0^2 - \left(\alpha_{i'}^2+\beta_{i'}^2\right)} e^{jk\frac{\alpha_{i'}^2+\beta_{i'}^2}{z_0}} \int_V \frac{\rho(x,y,z)}{16\pi^2 D_{T_i} D_{R_{i'}}} e^{-jk\left(D_{T_i}+D_{R_{i'}}\right)} dV$$

$$= \int_V \frac{\rho(x,y,z)}{16\pi^2 D_{T_i} D_{R_{i'}} \dfrac{z_0^2 - \left(\alpha_{i'}^2+\beta_{i'}^2\right)}{z_0^2}} e^{-jk\left(D_{T_i}+D_{R_{i'}}-\frac{\alpha_{i'}^2+\beta_{i'}^2}{z_0}\right)} dV \qquad (27)$$

$$= \int_V \frac{\rho(x,y,z)}{16\pi^2 \breve{D}_{C_{i'}}} e^{-jk\tilde{D}_{C_{i'}}} dV = \int_V \frac{\rho(x,y,z)}{16\pi^2 D_{C_{i'}}^2} e^{-j2kD_{C_{i'}}} dV.$$

$$\breve{D}_{C_{i'}} \simeq D_{T_i} D_{R_{i'}} \left[1 - \frac{\alpha_{i'}\left(x-x_{T_i}\right)+\beta_{i'}\left(y-y_{T_i}\right)-\dfrac{\alpha_{i'}^2}{2}-\dfrac{\beta_{i'}^2}{2}}{D_{T_i}^2} + \frac{\alpha_{i'}\left(x-x_{R_{i'}}\right)+\beta_{i'}\left(y-y_{R_{i'}}\right)+\dfrac{\alpha_{i'}^2}{2}+\dfrac{\beta_{i'}^2}{2}}{D_{R_{i'}}^2} \right.$$

$$- \frac{\left(\alpha_{i'}\left(x-x_{T_i}\right)+\beta_{i'}\left(y-y_{T_i}\right)\right)^2}{2D_{T_i}^4} - \frac{\left(\alpha_{i'}\left(x-x_{R_{i'}}\right)+\beta_{i'}\left(y-y_{R_{i'}}\right)\right)^2}{2D_{R_{i'}}^4} \qquad (24)$$

$$\left. - \frac{\alpha_{i'}^2\left(x-x_{T_i}\right)\left(x-x_{R_{i'}}\right)+\beta_{i'}^2\left(y-y_{T_i}\right)\left(y-y_{R_{i'}}\right)+\alpha_{i'}\beta_{i'}\left(\left(x-x_{T_i}\right)\left(y-y_{R_{i'}}\right)+\left(x-x_{R_{i'}}\right)\left(y-y_{T_i}\right)\right)}{D_{T_i}^2 D_{R_{i'}}^2} \right].$$

Note that in the above equation, the complex term $z_0^2 e^{jk\frac{\alpha_{i'}^2+\beta_{i'}^2}{z_0}}\Big/\left(z_0^2-\left(\alpha_{i'}^2+\beta_{i'}^2\right)\right)$ is independent of x, y and z and can be transferred into the integral. Equation (27) clearly states that from this point on we can work on a 3D data that contains information of virtual channels instead of a 5D data.

By taking a 2D FT on the spatial dimensions of the virtual aperture and according to (27), the continuous signal $\tilde{H}\left(x_C,y_C;f\right)$ in the wavenumber domain can be expressed as follows:

$$\tilde{\mathcal{H}}\left(k_x,k_y;f\right) \triangleq \mathrm{FT}_{x_C,y_C}\left\{\tilde{H}\left(x_C,y_C;f\right)\right\}$$
$$= \int_{y_C}\int_{x_C} \tilde{H}\left(x_C,y_C;f\right)e^{-jk_x x_C}e^{-jk_y y_C}\,dx_C dy_C \qquad (28)$$
$$= \frac{1}{16\pi^2}\int_V \rho\left(x,y,z\right)\underbrace{\int_{y_C}\int_{x_C}\frac{e^{-j2kD_C}}{D_C^2}e^{-jk_x x_C}e^{-jk_y y_C}\,dx_C dy_C}_{I_1}\,dV.$$

where $D_C = \sqrt{\left(x-x_C\right)^2+\left(y-y_C\right)^2+z^2}$. By expressing the double integral I_1 in the particular oscillatory integral form [45, 46] with the aim of using the method of stationary phase (MSP) [45, 46], and performing some mathematical operations and simplifications, the result can be written as follows (full derivation details are given in Appendix):

$$I_1 \simeq \frac{j\pi}{kz}e^{-j\left(k_x x+k_y y+k_z z\right)}, \qquad (29)$$

where

$$k_z = \sqrt{4k^2-k_x^2-k_y^2}, \quad 4k^2-k_x^2-k_y^2 \geq 0. \qquad (30)$$

Note that unlike the conventional derivations of other versions of RMA such as [47-51], in which the amplitude term $1/D_C^2$, due to its less influence than the phase term and the simplification of the extraction, is either completely ignored or only its approximation, $1/D_C$, is considered, in the derivation process by MSP, we have fully considered both phase and amplitude terms. This makes the output of the integral I_1 closer to the actual value.

By substituting (29) into (28), we have

$$\breve{\mathcal{H}}\left(k_x,k_y,k_z\right) =$$
$$\frac{j}{8\pi\sqrt{k_x^2+k_y^2+k_z^2}}\int_V \frac{\rho\left(x,y,z\right)}{z}e^{-j\left(k_x x+k_y y+k_z z\right)}\,dV, \qquad (31)$$

Comparing (28) and (30) indicates a mapping from signal $\tilde{\mathcal{H}}\left(k_x,k_y,k\right)$ to signal $\breve{\mathcal{H}}\left(k_x,k_y,k_z\right)$. Such a mapping, which is done by considering the dispersion relation in (30), is called Stolt interpolation [52, 53]. Equation (31) can be rewritten in the following form:

$$\underbrace{\iiint_{z\ y\ x}\frac{\rho\left(x,y,z\right)}{z}e^{-j\left(k_x x+k_y y+k_z z\right)}\,dxdydz}_{I_2} =$$
$$-j8\pi\sqrt{k_x^2+k_y^2+k_z^2}\,\breve{\mathcal{H}}\left(k_x,k_y,k_z\right), \qquad (32)$$

The term $-j8\pi\sqrt{k_x^2+k_y^2+k_z^2}$ acts as a filter in the Fourier domain applied to the signal $\breve{\mathcal{H}}\left(k_x,k_y,k_z\right)$. Now let us define $\rho'\left(x,y,z\right) \triangleq \rho\left(x,y,z\right)/z$ and $\mathcal{H}'\left(k_x,k_y,k_z\right) \triangleq -j8\pi\sqrt{k_x^2+k_y^2+k_z^2}\,\breve{\mathcal{H}}\left(k_x,k_y,k_z\right)$. Therefore, the signal $\rho'\left(x,y,z\right)$ can be obtained by applying a 3D inverse FT (IFT) to I_2. As a result, according to the relationship between $\rho\left(x,y,z\right)$ and $\rho'\left(x,y,z\right)$, we have

$$\rho\left(x,y,z\right) = z\mathrm{FT}^{-1}_{k_x,k_y,k_z}\left\{\mathcal{H}'\left(k_x,k_y,k_z\right)\right\}. \qquad (33)$$

III. RESULTS AND DISCUSSION

In this section, the performance of the proposed approach is evaluated by numerical simulations in MATLAB. All computations are performed in MATLAB R2022b running on a 64-bit Windows 11 operating system with 16 GB of random-access memory and a Core-i7 central processing unit at 2.8 GHz. Wherever not mentioned, the values of the main simulation parameters are as in Table I, where λ is the wavelength corresponding to the highest frequency in free space, N_f represents the number of uniformly distributed frequency samples, and D_z is the length of target space in the range direction. The value of the frequency sample step, which depends on the bandwidth and N_f, satisfies the condition of the Nyquist theorem [47]. Also, according to the values in

TABLE I
VALUES OF SIMULATION PARAMETERS

Parameter	$N_{T_x}=N_{T_y}=N_{R_x}=N_{R_y}$	$d_{T_x}=d_{T_y}$	$d_{R_x}=d_{R_y}$	f	N_f	z_0	D_z	L	$d_{i'}$
Value	11	56.86 mm ($11\lambda/2$)	5.17 mm ($\lambda/2$)	18-29 GHz	71	0.5 m	0.75 m	128	0

Table I, the theoretical resolutions of cross-range and range [50] are approximately equal to 1.03 cm and 1.36 cm respectively. In GA simulations, the value of constraint tolerance and the maximum number of generations [54, 55] are considered equal to 10^{-6} and 1000, respectively. In the simulations only related to extracting the backscatter frequency response (Examples 1 and 2), a provision has been made to evaluate the performance of the proposed approach independently of any particular scene. In these cases, the evaluation criterion is the frequency response normalized mean square error (FRNMSE), which can be calculated as follows [16]:

$$\text{FRNMSE} = \frac{\mathbb{E}\left\{\left(\hat{\mathbf{H}}_{i'} - \mathbf{H}_{i'}\right)^{H}\left(\hat{\mathbf{H}}_{i'} - \mathbf{H}_{i'}\right)\right\}}{\mathbb{E}\left\{\mathbf{H}_{i'}^{H}\mathbf{H}_{i'}\right\}}. \tag{35}$$

Also, the amplitudes of the simulated channels have a Weibull distribution with the values of the shape parameter and scaling parameter equal to 1.8 and 0.975, respectively, so that $\mathbb{E}\left\{\left|H_{i,i'}\left(f\right)\right|^{2}\right\} = 1$ [16, 56]. It has been demonstrated that such a distribution provides a good fit for the statistical modeling of the indoor radio propagation channel [56]. Channel phases are modeled as uniformly distributed in $\left[0, 2\pi\right)$.

Example 1: In the first experiment, we evaluate the performance of optimizing code sequences, which were proposed in Section II-B-1. Fig. 3 shows the maximum values of the aperiodic ACF for the original sequences and optimized sequences for code lengths of 32 and 128. As can be seen, after the optimization process, the temporal correlation properties of the sequences have been improved. In addition to aperiodic ACF, based on the obtained vector $\mathbf{x}$, the behavior of maximum values of aperiodic cross-correlation functions (CCF) was also investigated. The corresponding results are shown in Fig. 4, which are again a confirmation of the improvement of the aforementioned features after optimization. Moreover, we have calculated the average FRNMSE values in 400 independent Monte-Carlo runs, the results of which are given for different symbol-energy-to-noise-spectral-density ratios (E_s/N_0 s) in Fig. 5. Lags are considered as a discrete uniform random distribution in $\left[1, L-1\right]$. The effect of the optimization process in improving the FRNMSE values is clear in Fig. 5.
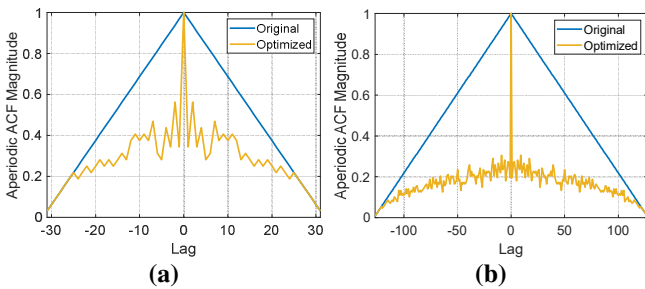
Fig. 3. Maximum values of aperiodic ACF for original sequences and optimized sequences; **(a)** for $L = 32$, **(b)** for $L = 128$.
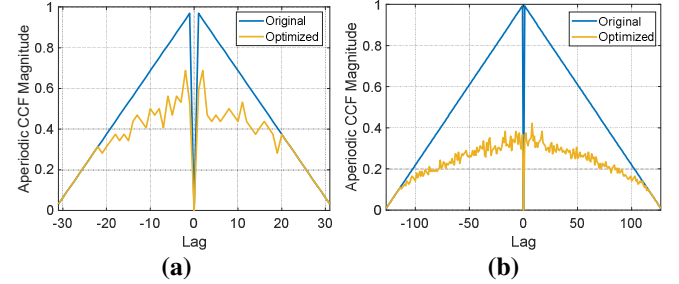
Fig. 4. Maximum values of aperiodic CCF for original sequences and optimized sequences; **(a)** for $L = 32$, **(b)** for $L = 128$.
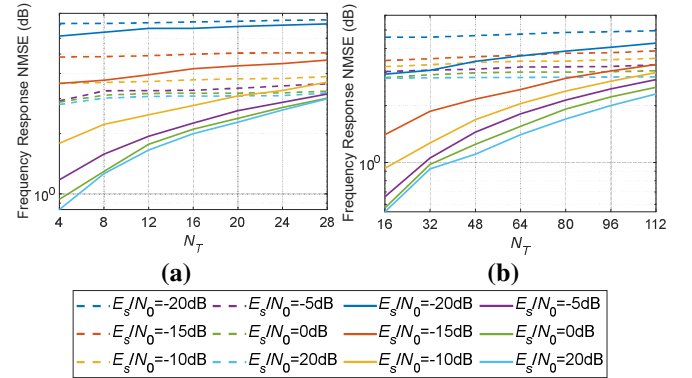

Fig. 5. The effect of improving the temporal correlation properties of the code sequences on the improvement of the FRNMSE values; **(a)** for $L = 32$, **(b)** for $L = 128$. Dashed lines and solid lines are associated with the original and optimized sequences, respectively.

Example 2: In the second example, the performance of the proposed approach is compared with the conventional approach (without coding the transmitted signals (assuming temporal orthogonality)) by the FRNMSE criterion in terms of code length, number of Tx antennas, and DC offset. The results are obtained based on the average of 400 independent executions. Fig. 6 shows the outputs for varying code lengths when N_T is fixed at 3. It can be seen that the outputs of the proposed approach (solid lines) are always superior to the corresponding outputs in a single Tx case without any coding (dashed lines). This is due to the additional coding gain, because in the first case, the noise power is averaged over L measurements. Mathematically, this means that the FRNMSE is equal to the estimated variance σ_n^2/L, where σ_n^2 represents the measurement noise variance (see [16] for more details). This is why in the case of solid lines, when the length of the code increases, the error decreases. The error reduction rate is consistent with the above theoretical analysis (see Fig. 6 where the solid lines are almost identical with the dotted lines). Now let us consider the code length as fixed and examine the FRNMSE changes versus N_T. The results for

different values of E_s/N_0 are shown in Fig. 7. Similar to Fig. 6, it was expected that the outputs related to the coded signals scenario (solid lines) would show lower error values. It can also be seen from Fig. 7 that the error values are independent of the number of Tx antennas. The reason for this is the mutual orthogonality between the codes of different Txs. In the next experiment, we investigate the performance of orthogonal coding in the proposed approach on suppressing unwanted complex DC offsets. Fig. 8 shows the output of the simulations (FRNMSE) for different values of versus $|d_{i'}|$, where the phase of $d_{i'}$ is considered as a uniform random distribution in $[0, 2\pi)$. It can be seen that the outputs related to the proposed approach are independent of the DC offset value and are only affected by E_s/N_0. This is due to the balanced property in $\tilde{\mathbf{W}}$, which was analytically pointed out after (10). Unlike the scheme based on orthogonal coding, it can be seen in Fig. 8 that the single Tx mode without any coding is prone to distortion caused by DC offset in channel estimation. In the latter case, there are breakpoints, after which the error values start to increase. These points are the boundary of the dominance of DC offset to noise, which occur for $|d_{i'}| > 1/\sqrt{E_s/N_0}$ and change the value of FRNMSE from $1/\sqrt{E_s/N_0}$ to $|d_{i'}|^2$.
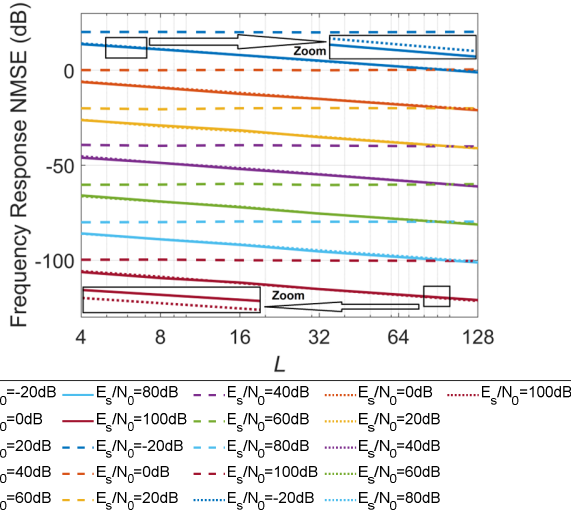
Fig. 6. Comparison of FRNMSE values versus code length. $N_T = 3$. Dashed lines, solid lines, and dotted lines are associated with the outputs without any coding, the outputs of the proposed approach and values of σ_n^2/L, respectively.
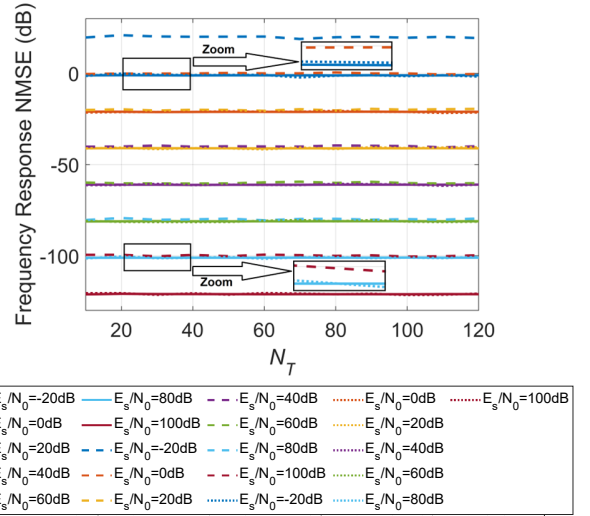

Fig. 7. Comparison of FRNMSE values versus the number of Txs. Dashed lines, solid lines, and dotted lines are associated with the outputs without any coding, the outputs of the proposed approach and the approximation of the estimated variance σ_n^2/L, respectively.
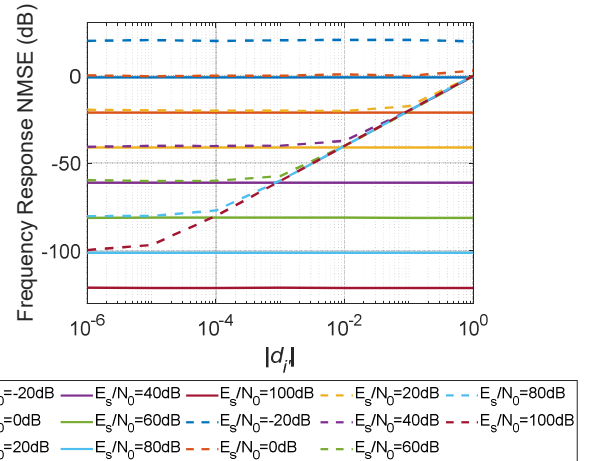
Fig. 8. Comparison of FRNMSE values versus $|d_{i'}|$. Dashed lines and solid lines are associated with the outputs without any coding and the outputs based on orthogonal coding in the proposed approach, respectively.

Example 3: In this example, a point scatterer located at $(0, 0, 0.4)$, in meters, is assumed as the target, resulting in a point spread function (PSF). Two URAs with sizes of 9×9 are considered and the inter-element spacings in them are determined according to the explanation given in Section II-A. The reconstructed images obtained by using the proposed CGRDF algorithm for different values of E_s/N_0 are shown in Fig. 9. It can be seen that in all cases, the location of the target in the cross-range and range directions is correctly detected. However, as expected, with the decrease of E_s/N_0, the difference between the peak and the floor of the normalized signal corresponding to the reconstructed image decreases (in other words, the desired signal is more drowned in noise).

Note that since in this example all the conditions in the x and y directions are the same, for cross-range views, only the reconstructed PSF display in the x direction is provided.
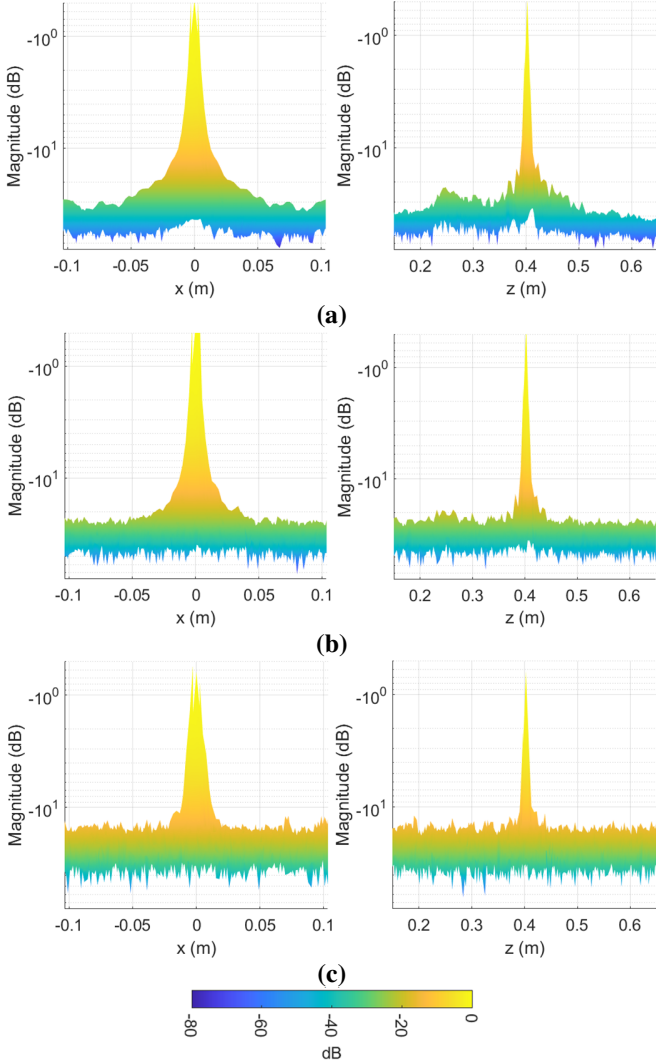

Fig. 9. The normalized reconstructed PSFs (in cross-range and range directions) by employing the proposed CGRDF algorithm; **(a)** $E_s/N_0 = 20\,\text{dB}$, **(b)** $E_s/N_0 = 0\,\text{dB}$, **(c)** $E_s/N_0 = -10\,\text{dB}$.

Example 4: In this example, the performance of the proposed algorithm is investigated from the point of view of the effect of the derived terms and the approximations used on the results, as well as the resolution. It is assumed that three point scatterers are located at positions $(-0.05, -0.04, 0.46)$, $(0, 0, 0.5)$ and $(0.05, 0.04, 0.54)$, all in meters.

First, the effect of fully taking into account the amplitude terms, which were specially considered in the mathematical derivations of the proposed CGRDF algorithm, is shown on the outputs related to multiple specific targets. Fig. 10(a) shows the image reconstructed by the proposed algorithm (in 3D and 2D views) when the derived amplitude terms (range compensators in (33) and (25) and smoothing filter in (32)) are

ignored. In Fig. 10(a), it can be seen that the farthest target is not detected. The reason for this is the propagation loss effect, which is a well-known issue in conventional RMA-based techniques [13, 42]. Fig. 10(b) shows the output of the proposed approach by including the derived amplitude terms. As can be seen, applying the derived terms has been effective in relaxing the propagation loss effect, and now all three point targets can be identified. Note that although the distant targets may also be displayed by reducing the Isovalue, reducing it simultaneously increases the strength of the sidelobes, which is not desirable.
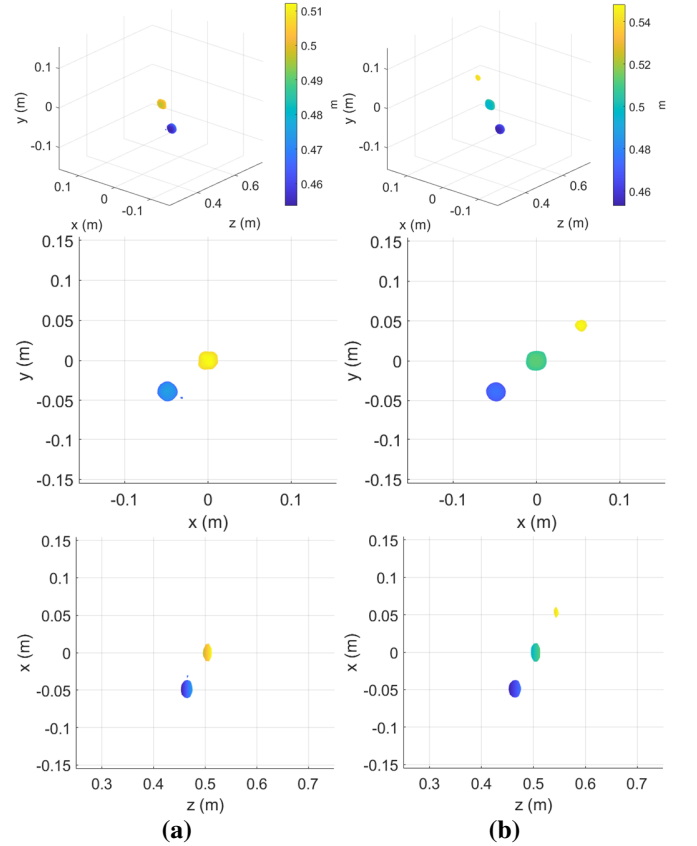

Fig. 10. The isosurfaces of the images reconstructed by the proposed approach in 3D and 2D views; **(a)** when the derived amplitude terms are ignored, **(b)** when the derived amplitude terms are fully included. Isovalue: -10 dB.

Now, let us examine the effect of the target being too close to the aperture, assuming other parameters remain unchanged. Figs. 11(a) and 11(b) show the outputs of the proposed approach when z_0 is equal to 0.3 m and 0.25 m, respectively. By comparing these figures and Fig. 10(b), it can be seen that distortions appear in the reconstructed target by getting closer to the aperture. Such behavior can be expected at ranges too close to the aperture, due to some approximations used in the derivations of Section II-C.
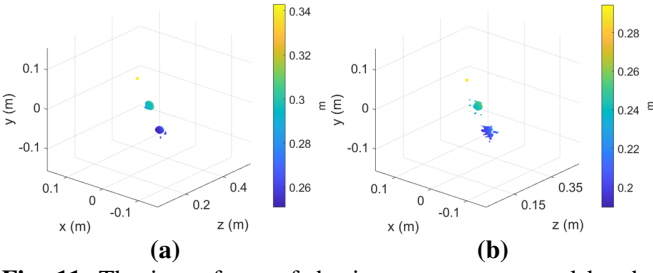
Fig. 11. The isosurfaces of the images reconstructed by the proposed approach in Example 4; **(a)** when $z_0 = 0.3\,\mathrm{m}$, **(b)** when $z_0 = 0.25\,\mathrm{m}$. Isovalue: -10 dB.

To evaluate the resolutions in the proposed approach, we brought the point scatterers close to each other to the extent that they can be separated from each other and extracted the corresponding mesh surface PSF plots for greater clarity. Figs. 12(a), 12(b), and 12(c) show the reconstructed images focused at a range of 0.5 m when the point scatterers are separated by a distance of 1.9, 1.8, and 1.7 cm from each other in the x and y directions, respectively. The range of the targets is 0.5 meters. By considering the -3 dB full-width at half-maximum (FWHM) criterion to determine the resolution [57], at 1.7 cm separation, it can be seen that the PSF main lobes of the point scatterers remain above the -3 dB width, setting the cross-range resolution limit. Although it is naturally expected that the resolution values in practice are larger than the corresponding theoretical values, here the difference between the practical value (1.7 cm) and the theoretical value (1.03 cm as mentioned at the beginning of Section III) might seem slightly larger than expected. This is due to the close range of the targets to the aperture. In fact, as discussed in the previous paragraph, due to the approximations used in the extraction of NF terms, the closer we get to the aperture, the more distortions and errors we expect to encounter (compared to distances farther from the aperture). To confirm this aspect of the cross-range resolution, we repeated the above test, this time at a range of 1 m. Obviously, the theoretical resolution is doubled (i.e. 2.06 cm), because it has a direct linear relationship with the range. The results are shown in Figs. 12(d)-12(f). By observing the -3 dB FWHM of the PSF main lobes, a resolution of 2.2 cm can be obtained for the proposed approach, which is much closer to the corresponding theoretical value. A similar experiment (this time by fixing the horizontal and vertical position of the targets at $(0,0)$ and changing the range of the two side targets) was conducted to evaluate the range resolution, the results of which are shown in Fig. 13. According to the obtained plots, a range resolution of 2 cm is provided (while the corresponding calculated theoretical value is 1.36 cm).
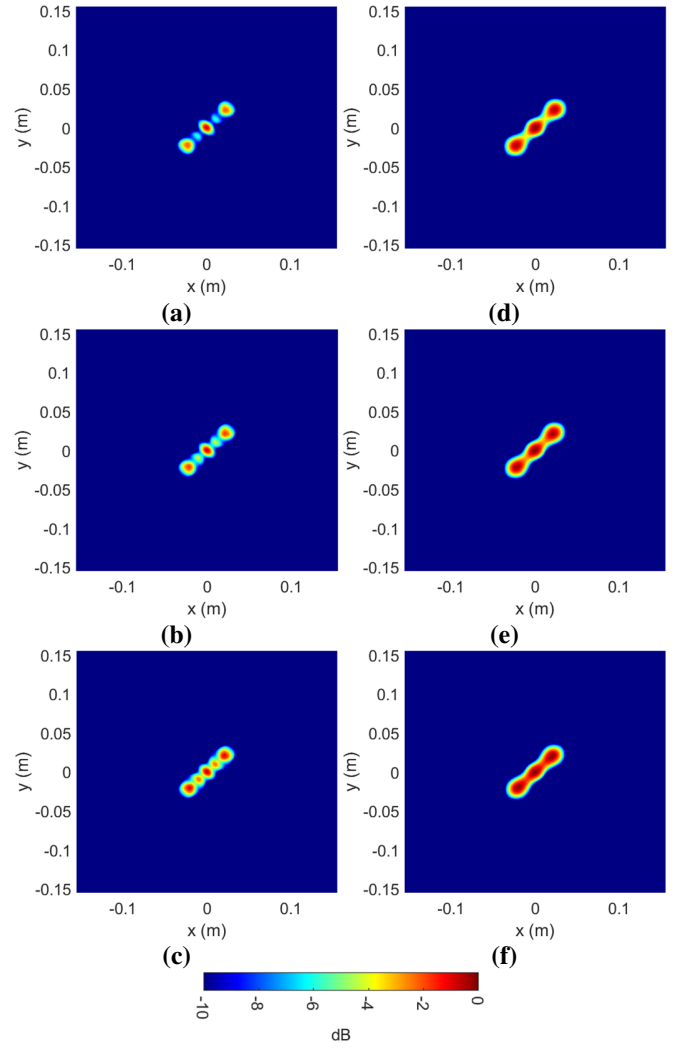
Fig. 12. Mesh surface plots of reconstructed images (focused in the ranges of 0.5 and 1 m for the left and right columns, respectively) by employing the proposed CGRDF algorithm when the targets are located at **(a)** $(-0.019, -0.019, 0.5)$, $(0,0,0.5)$ and $(0.019, 0.019, 0.5)$, **(b)** $(-0.018, -0.018, 0.5)$, $(0,0,0.5)$ and $(0.018, 0.018, 0.5)$, **(c)** $(-0.017, -0.017, 0.5)$, $(0,0,0.5)$ and $(0.017, 0.017, 0.5)$, **(d)** $(-0.023, -0.023, 1)$, $(0,0,1)$ and $(0.023, 0.023, 1)$, **(e)** $(-0.022, -0.022, 1)$, $(0,0,1)$ and $(0.022, 0.022, 1)$, **(f)** $(-0.021, -0.021, 1)$, $(0,0,1)$ and $(0.021, 0.021, 1)$, all in meters.

Example 5: In the last experiment, the performance of the proposed approach is compared with other techniques. A T-shaped distributed target with dimensions of $0.099 \times 0.099 \times 0.01\,\mathrm{m}^3$ is considered (see Fig. 14). The number of voxels to define the scene is $121 \times 121 \times 146$. According to the values in Table I as well as the Nyquist criterion [58], the conditions required for spatial sampling in the x and y directions in order to avoid aliasing, i.e.

$d_x \leq 0.5\lambda \sqrt{\left(L_x^v + L_x^t\right)^2 \Big/ 4 + z_0^2} \Big/ \left(L_x^v + L_x^t\right)$ and

$d_y \leq 0.5\lambda \sqrt{\left(L_y^v + L_y^t\right)^2 \Big/ 4 + z_0^2} \Big/ \left(L_y^v + L_y^t\right)$, where λ, z_0, L_x^v, L_y^v, L_x^t and L_y^t represent wavelength corresponding to the highest frequency in free space, range in the center of the scene, and sizes of the virtual aperture and the scene (see Fig. 1(b)), respectively, are met in the proposed algorithm. Fig. 15 shows the reconstructed images by the generalized synthetic aperture focusing technique (GSAFT) [8, 59], the method [16] and the proposed algorithm. The target image is clearly identifiable in all three outputs. However, visually, the outputs of the first two methods seem to be of higher quality and more like the original target image form in Fig. 10. In addition, Table II quantitatively confirms that the reconstructed images by GSAFT and method [16] are similar in terms of quality. In Table II, once Fig. 15(a) and once Fig. 15(b) are considered as reference images, and the corresponding reconstructed image NMSE (RINMSE) values are calculated for them as [13]:

RINMSE =

$$\frac{\sum_{q=1}^{N_x'} \sum_{q'=1}^{N_y'} \sum_{q''=1}^{N_z'} \left| \rho_{\mathrm{Rec}}\left(x_q, y_{q'}, z_{q''}\right) - \rho_{\mathrm{Ref}}\left(x_q, y_{q'}, z_{q''}\right)\right|^2}{\sum_{q=1}^{N_x'} \sum_{q'=1}^{N_y'} \sum_{q''=1}^{N_z'} \left| \rho_{\mathrm{Ref}}\left(x_q, y_{q'}, z_{q''}\right)\right|^2}, \quad (36)$$

where ρ_{Rec} and ρ_{Ref} denote the reconstructed image and reference image. Also, the image contrast (IC) values in Table II are calculated in the following form [13]:

$$\mathrm{IC}(I) = I_{\max} - I_{\min}, \quad (37)$$

where $I_{\max}$ and $I_{\min}$ respectively represent the maximum and minimum value intensities in image I obtained based on the corresponding values averaged from the reconstructed 2D images (in the xy-plane) focused on different ranges (when the pixel values are normalized by dividing by 255). Quantitative comparisons in Table II are consistent with visual findings from Fig. 15.
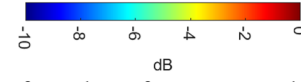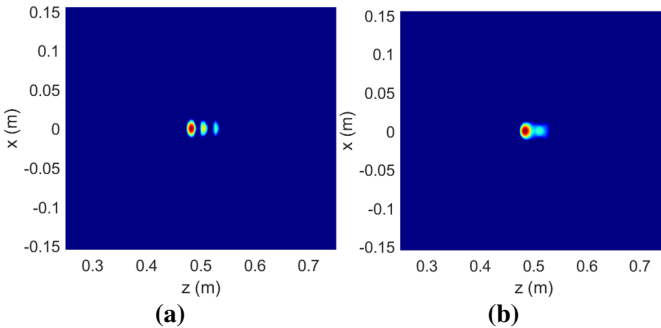

Fig. 13. Mesh surface plots of reconstructed images focused at $y = 0$ m by employing the proposed CGRDF algorithm when the targets are located at **(a)** $(0,0,0.48)$, $(0,0,0.5)$ and $(0,0,0.52)$, **(b)** $(0,0,0.481)$, $(0,0,0.5)$ and $(0,0,0.519)$, all in meters.
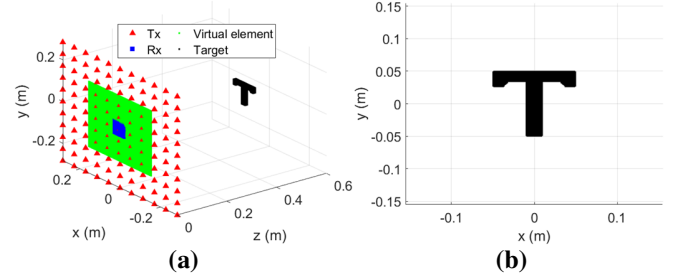

Fig. 14. General imaging configuration in Example 5; (a) 3D view of the aperture and target structure, (b) 2D view of the T-shaped target.

The noteworthy point is the computational time required to implement the above algorithms. Table II indicates that the proposed CGRDF algorithm has reconstructed an understandable image of the scene after about one second, while the computation time for GSAFT and method [16] is more than 1000 seconds, which is not optimal for real-time applications. Although computational time can provide a preliminary idea of computational efficiency, computational complexity provides a more reliable picture. The total computational complexity of the proposed algorithm, considering the major multiplications involved in extracting the transfer function, Fourier calculations and the interpolation process, is given in (38), where N_p represents the order of the multiplicative complexity for one Stolt's mapping [60]. The total computational complexity of CGRDF in terms of the number of frequency samples and the number of antennas is plotted in Fig. 16 and compared with the complexities of the GSAFT, the method [16] and the conventional MIMO RMA (for the details on the computational complexity of the mentioned methods, refer to [10, 13, 61]). It can be seen that the method [16] (due to the use of an LS-based approach) and the GSAFT algorithm have very high complexity. Also, Fig. 16 demonstrates that the CGRDF algorithm has better computational performance even compared to MIMO RMA that is a Fourier-based scheme. The main reason for this is the reduction of Stolt interpolation stage calculations (migration from 5D-to-3D interpolation to 3D-to-3D one).

$$\mathcal{O}\left(N_f N_T N_R L + N_f N_T N_R \log_2\left(N_T N_R\right) + N_x' N_y' N_p + N_x' N_y' N_z' \log_2\left(N_x' N_y' N_z'\right)\right) \quad (38)$$
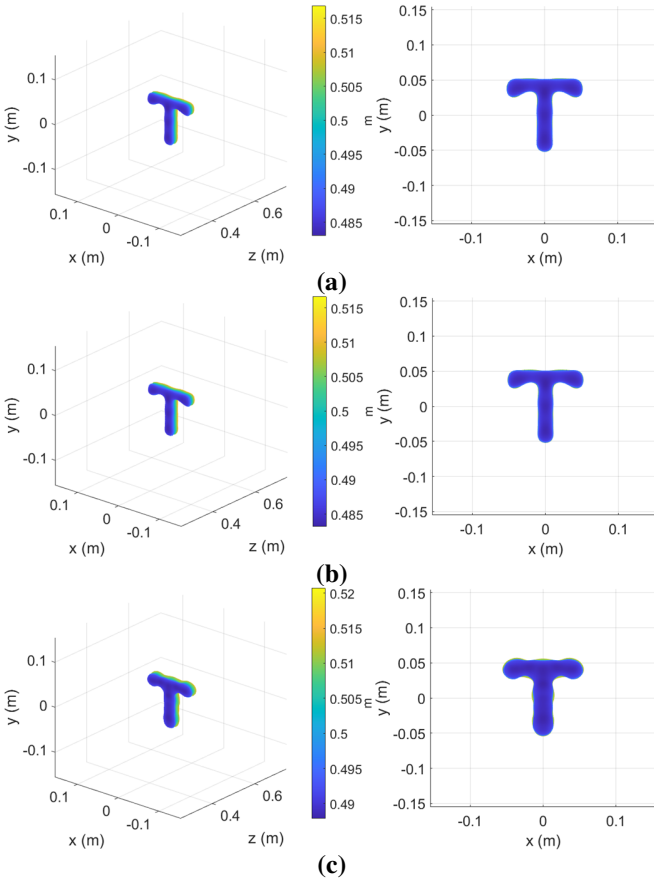
Fig. 15. The isosurfaces of the reconstructed images of a T-shaped target; **(a)** by GSAFT technique, **(b)** by method [16], **(c)** by proposed CGRDF algorithm. Isovalue: -10 dB.
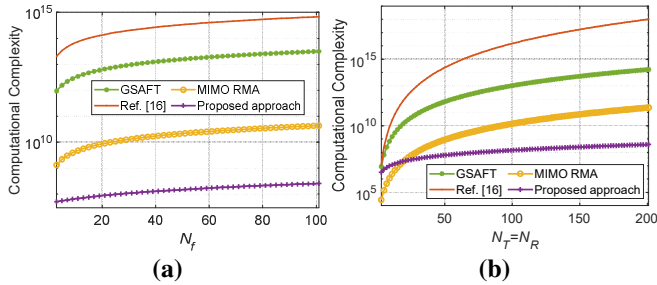
Fig. 16. Comparison of computational complexity in different algorithms; **(a)** versus the number of frequency samples, **(b)** versus the number of antennas.

IV. CONCLUSION

In this paper, with the aim of sensing scene information with the simultaneous operation of all Txs, an approach based on optimal orthogonal coding was presented in a NF multistatic imaging scenario. In particular, a specific MIMO configuration was introduced, through which, in the above scenario, it was possible to map 4D to 2D spatial data compatible with fast Fourier calculations. After introducing the model of the transmitted and received signals, the method of extracting the paired information of Tx-Rx channels was presented. Then, a low-cost computational algorithm was derived mathematically according to the data extracted from the channel information, taking into account all terms of phases and amplitudes. The performance of the proposed approach was evaluated in various experiments with qualitative measures of reconstructed images, as well as quantitative measures of ACF, CCF, FRNMSE, RINMSE, computational time and computational complexity. The results of numerical simulations showed that the proposed approach is able to meet the requirements of reliable real-time imaging.

In this work, beyond image reconstruction, the aspects of waveform diversity and retrieval of individual channel data in an imaging system were also considered. The scheme of simultaneous transmission of orthogonal signals by multiple Txs was used only for sensing. In the current model, it is possible to extract the channel transfer function on the Rx side (mathematically, in (8), an estimate of $\mathbf{H}_{i'}(f)$ can be calculated). For the purpose of sensing considered in this paper, there is no need to retrieve $\tilde{\mathbf{W}}$ (see (8)). But from another point of view, if we look at $\tilde{\mathbf{W}}$ as a message, its retrieval at the Rx side means that communication is achieved. The development of the current model to integrate sensing and communication functions [62, 63] will be considered as future work.

APPENDIX

Details of solving the integral I_1: The integral I_1 in (28) can be asymptotically evaluated using MSP [64]. This method can be used to obtain an analytical solution for integrals in the general form of the left side of the following equation [65]:

$$\iint g(x, y) e^{jk\Theta(x, y)} dxdy \simeq \frac{j2\pi\sigma}{\sqrt{|\eta\iota - \gamma^2|}k} g(x_0, y_0) e^{jk\Theta(x_0, y_0)}, (39)$$

where the domain of integration is determined by the aperture and the stationary phase position (x_0, y_0) [66] is obtained by finding the zeros of the first derivative of the exponential term argument; that is,

TABLE II
QUANTITATIVE COMPARISON OF PERFORMANCE OF DIFFERENT METHODS CORRESPONDING TO FIG. 15

Approach	RINMSE 1	RINMSE 2	IC	Computational Time
GSAFT	0.00051	Reference image	136.74	1044 Sec
[16]	Reference image	0.0005	141.94	1679 Sec
Proposed	0.92	0.9	125.71	0.93 Sec

$$\left.\frac{\partial\Theta}{\partial x}\right|_{(x_0,y_0)} = \left.\frac{\partial\Theta}{\partial y}\right|_{(x_0,y_0)} = 0. \tag{40}$$

Also, in (39), $\eta = \partial^2\Theta/\partial x^2\big|_{(x_0,y_0)}$, $\iota = \partial^2\Theta/\partial y^2\big|_{(x_0,y_0)}$ and $\gamma = \partial^2\Theta/\partial x\partial y\big|_{(x_0,y_0)}$, and [65]

$$\sigma = \begin{cases} 1, & \eta\iota > \gamma^2, \eta > 0, \\ -1, & \eta\iota > \gamma^2, \eta < 0, \\ -1, & \eta\iota < \gamma^2. \end{cases} \tag{41}$$

By comparing the integral I_1 in (28) with the form (39), it can be written

$$I_1 = \iint_{y_C\,x_C} g(x_C, y_C) e^{jk\Theta(x_C, y_C)} dx_C dy_C \tag{42}$$

where $g(x_C, y_C) = 1/D_C^2$ and $\Theta(x_C, y_C) = -2D_C - k_x/k\, x_C - k_y/k\, y_C$. The first partial derivatives of the phase function are

$$\begin{aligned} \frac{\partial\Theta}{\partial x_C} &= 2\frac{x - x_C}{D_C} - \frac{k_x}{k}, \\ \frac{\partial\Theta}{\partial y_C} &= 2\frac{y - y_C}{D_C} - \frac{k_y}{k}, \end{aligned} \tag{43}$$

and from them, the required second partial derivatives are obtained, which after some algebraic simplifications we have

$$\begin{aligned} \frac{\partial^2\Theta}{\partial x_C^2} &= -2\frac{(y - y_C)^2 + z^2}{D_C^3}, \\ \frac{\partial^2\Theta}{\partial y_C^2} &= -2\frac{(x - x_C)^2 + z^2}{D_C^3}, \\ \frac{\partial^2\Theta}{\partial x_C y_C} &= 2\frac{(x - x_C)(y - y_C)}{D_C^3}. \end{aligned} \tag{44}$$

Now it is necessary to calculate the stationary phase position according to (40). So, we have

$$\left.\frac{\partial\Theta}{\partial x_C}\right|_{(x_0,y_0)} = 0 \;\Rightarrow\; 2\frac{x - x_0}{D_C\big|_{(x_0,y_0)}} = \frac{k_x}{k}, \tag{45}$$

$$\left.\frac{\partial\Theta}{\partial y_C}\right|_{(x_0,y_0)} = 0 \;\Rightarrow\; 2\frac{y - x_0}{D_C\big|_{(x_0,y_0)}} = \frac{k_y}{k}, \tag{46}$$

Equations (45) and (46) after some simplifications lead to (47)

and (48), respectively

$$(x - x_0)^2 = \frac{(y - y_0)^2 + z^2}{4k^2 - k_x^2} k_x^2, \tag{47}$$

$$(y - y_0)^2 = \frac{(x - x_0)^2 + z^2}{4k^2 - k_y^2} k_y^2. \tag{48}$$

To obtain the two unknowns x_0 and y_0 by using the above two equations, we substitute (48) in (47) as follows:

$$\begin{aligned} (x - x_0)^2 &= \frac{\dfrac{(x - x_0)^2 + z^2}{4k^2 - k_y^2} k_y^2 + z^2}{4k^2 - k_x^2} k_x^2 \\ &= \frac{k_y^2\left((x - x_0)^2 + z^2\right) + z^2\left(4k^2 - k_y^2\right)}{\left(4k^2 - k_x^2\right)\left(4k^2 - k_y^2\right)} k_x^2 = \frac{z^2 k_x^2}{4k^2 - k_x^2 - k_y^2}. \end{aligned} \tag{49}$$

By extracting the positive root of the above equation, we have

$$x_0 = x - \frac{k_x}{\sqrt{4k^2 - k_x^2 - k_y^2}} z. \tag{50}$$

In a similar way, we can get y_0 which becomes

$$y_0 = y - \frac{k_y}{\sqrt{4k^2 - k_x^2 - k_y^2}} z. \tag{51}$$

Since x_0 and y_0 must be real values, as a result, the frequency wavenumber must satisfy the inequality $4k^2 - k_x^2 - k_y^2 \geq 0$.

Finally, it is necessary to evaluate the functions g, Θ, η, ι and γ in the stationary phase position. The outputs after mathematical simplifications are given below

$$\begin{aligned} g(x_0, y_0) &= \frac{4k^2 - k_x^2 - k_y^2}{4k^2 z^2}, \\ \Theta(x_0, y_0) &= -\frac{k_x}{k} x - \frac{k_y}{k} y - \frac{\sqrt{4k^2 - k_x^2 - k_y^2}}{k} z, \\ \eta(x_0, y_0) &= -\frac{\left(4k^2 - k_x^2\right)\sqrt{4k^2 - k_x^2 - k_y^2}}{4k^3 z}, \\ \iota(x_0, y_0) &= -\frac{\left(4k^2 - k_y^2\right)\sqrt{4k^2 - k_x^2 - k_y^2}}{4k^3 z}, \\ \gamma(x_0, y_0) &= \frac{k_x k_y \sqrt{4k^2 - k_x^2 - k_y^2}}{4k^3 z}. \end{aligned} \tag{52}$$

Also, we have

$$\eta(x_0, y_0)\iota(x_0, y_0) = \frac{(4k^2 - k_x^2)(4k^2 - k_y^2)(4k^2 - k_x^2 - k_y^2)}{16k^6 z^2}, \quad (53)$$

$$\gamma^2(x_0, y_0) = \frac{k_x^2 k_y^2(4k^2 - k_x^2 - k_y^2)}{16k^6 z^2}.$$

As a result,

$$\eta(x_0, y_0)\iota(x_0, y_0) - \gamma^2(x_0, y_0) = (4k^2 - k_x^2 - k_y^2)^2 \big/ (4k^4 z^2),$$

which always returns a positive value. Also, according to (44), η is always a negative value. Therefore, by considering (41), σ must be 1. Finally, according to (39), (42), (52) and (53), as well as the above points, the integral I_1 can be approximated in the following form:

$$I_1 \simeq \frac{j2\pi}{\sqrt{(4k^2 - k_x^2 - k_y^2)^2 \big/ (4k^4 z^2)} \, k} \frac{4k^2 - k_x^2 - k_y^2}{4k^2 z^2}$$

$$\times e^{jk\left(-\frac{k_x}{k}x - \frac{k_y}{k}y - \frac{\sqrt{4k^2 - k_x^2 - k_y^2}}{k}z\right)} \quad (54)$$

$$= \frac{j\pi}{kz} e^{-j\left(k_x x + k_y y + \sqrt{4k^2 - k_x^2 - k_y^2}\, z\right)}, \quad 4k^2 - k_x^2 - k_y^2 \geq 0.$$

References

[1] Y. El Masri and T. Rakha, "A scoping review of non-destructive testing (NDT) techniques in building performance diagnostic inspections," *Construction and Building Materials,* vol. 265, p. 120542, 2020.

[2] W. Shao and T. McCollough, "Advances in microwave near-field imaging: Prototypes, systems, and applications," *IEEE microwave magazine,* vol. 21, no. 5, pp. 94-119, 2020.

[3] A. M. Molaei, V. Skouroliakou, V. Fusco, and O. Yurduseven, "Efficient 3D Image Reconstruction for Near-Field Microwave Imaging Using Dynamic Metasurface Antenna," *IEEE Access,* vol. 10, pp. 68491-68498, 2022.

[4] N. Rojhani, M. Passafiume, M. Lucarelli, G. Collodi, and A. Cidronali, "Assessment of Compressive Sensing 2× 2 MIMO Antenna Design for Millimeter-Wave Radar Image Enhancement," *Electronics,* vol. 9, no. 4, p. 624, 2020.

[5] Y.-F. Cheng, X. Ding, W. Shao, and C. Liao, "A high-gain sparse phased array with wide-angle scanning performance and low sidelobe levels," *IEEE Access,* vol. 7, pp. 31151-31158, 2019.

[6] T. Torres, N. Anselmi, P. Nayeri, P. Rocca, and R. Haupt, "Low discrepancy sparse phased array antennas," *Sensors,* vol. 21, no. 23, p. 7816, 2021.

[7] A. M. Molaei, S. Hu, V. Skouroliakou, V. Fusco, X. Chen, and O. Yurduseven, "Fourier compatible near-field multiple-input multiple-output terahertz imaging with sparse non-uniform apertures," *IEEE Access,* vol. 9, pp. 157278-157294, 2021.

[8] S. Hu *et al.*, "Multistatic MIMO Sparse Imaging Based on FFT and Low-Rank Matrix Recovery Techniques," *IEEE Transactions on Microwave Theory and Techniques,* 2022.

[9] M. Alibakhshikenari *et al.*, "Metamaterial-inspired antenna array for application in microwave breast imaging systems for tumor detection," *IEEE Access,* vol. 8, pp. 174667-174678, 2020.

[10] J. Wang, P. Aubry, and A. Yarovoy, "3-D short-range imaging with irregular MIMO arrays using NUFFT-based range migration algorithm," *IEEE Transactions on Geoscience and Remote Sensing,* vol. 58, no. 7, pp. 4730-4742, 2020.

[11] E. Björnson, L. Sanguinetti, H. Wymeersch, J. Hoydis, and T. L. Marzetta, "Massive MIMO is a reality—What is next?: Five promising research directions for antenna arrays," *Digital Signal Processing,* vol. 94, pp. 3-20, 2019.

[12] A. Studenikin and A. Zhuk, "Software model for the synthesis of increased volumes of systems of discrete orthogonal code sequences," in *IOP Conference Series: Materials Science and Engineering*, 2021, vol. 1069, no. 1: IOP Publishing, p. 012039.

[13] A. M. Molaei, T. Fromenteze, S. Hu, V. Fusco, and O. Yurduseven, "Fourier-Based Near-Field Three-Dimensional Image Reconstruction in a Multistatic Imaging Structure Using Dynamic Metasurface Antennas," *IEEE Transactions on Computational Imaging,* vol. 8, pp. 1089-1100, 2022.

[14] A. M. Molaei, O. Yurduseven, and V. Fusco, "An efficient waveform diversity based on variational mode decomposition of coded beat-frequency shifted signals algorithm for multiple-input multiple-output millimetre-wave imaging," *IET Radar, Sonar & Navigation,* vol. 15, no. 10, pp. 1266-1280, 2021.

[15] A. M. Molaei, S. Hu, V. Fusco, and O. Yurduseven, "A multi-resolution analysis-based approach to accelerate data acquisition for near-field MIMO millimeter-wave imaging," in *Passive and Active Millimeter-Wave Imaging XXV*, 2022, vol. 12111: SPIE, pp. 90-101.

[16] A. Pedross-Engel *et al.*, "Orthogonal coded active illumination for millimeter wave, massive-MIMO computational imaging with metasurface antennas," *IEEE Transactions on Computational Imaging,* vol. 4, no. 2, pp. 184-193, 2018.

[17] P. R. Gill and D. G. Stork, "Computationally efficient Fourier-based image reconstruction in a lensless diffractive imager," in *Computational Optical Sensing and Imaging*, 2015: Optica Publishing Group, p. CM3E. 4.

[18] M. Abbasi, A. Shayei, M. Shabany, and Z. Kavehvash, "Fast Fourier-based implementation of synthetic aperture radar algorithm for multistatic imaging system," *IEEE Transactions on Instrumentation and Measurement,* vol. 68, no. 9, pp. 3339-3349, 2018.

[19] A. M. Molaei, R. Kumar, S. Hu, V. Skouroliakou, V. Fusco, and O. Yurduseven, "A Compressive Sensing-Based Approach for Millimeter-Wave Imaging Compatible with Fourier-Based Image Reconstruction Techniques," in *2022 23rd International Radar Symposium (IRS)*, 2022: IEEE, pp. 87-91.

[20] R. Yang *et al.*, *High-Resolution Microwave Imaging*. Springer, 2018.

[21] G. Wang, F. Qi, Z. Liu, C. Liu, C. Xing, and W. Ning, "Comparison between back projection algorithm and range migration algorithm in terahertz imaging," *IEEE Access,* vol. 8, pp. 18772-18777, 2020.

[22] J. Fortuny-Guasch and J. M. Lopez-Sanchez, "Extension of the 3-D range migration algorithm to cylindrical and spherical scanning geometries," *IEEE Transactions on Antennas and Propagation,* vol. 49, no. 10, pp. 1434-1444, 2001.

[23] T. Fromenteze, O. Yurduseven, F. Berland, C. Decroze, D. R. Smith, and A. G. Yarovoy, "A transverse spectrum deconvolution technique for MIMO short-range Fourier imaging," *IEEE Transactions on Geoscience and Remote Sensing,* vol. 57, no. 9, pp. 6311-6324, 2019.

[24] A. M. Molaei, S. Hu, V. Skouroliakou, V. Fusco, X. Chen, and O. Yurduseven, "Fast processing approach for near-field terahertz imaging with linear sparse periodic array," *IEEE Sensors Journal,* vol. 22, no. 5, pp. 4410-4424, 2022.

[25] A. M. Molaei, P. del Hougne, V. Fusco, and O. Yurduseven, "Efficient Joint Estimation of DOA, Range and Reflectivity in Near-Field by Using Mixed-Order Statistics and a Symmetric MIMO Array," *IEEE Transactions on Vehicular Technology,* vol. 71, no. 3, pp. 2824-2842, 2021.

[26] A. M. Molaei, P. Del Hougne, V. Fusco, and O. Yurduseven, "Numerical-Analytical Study of Performance of Mixed-Order Statistics Algorithm for Joint Estimation of DOA, Range and Backscatter Coefficient in a MIMO Structure," in *2022 23rd International Radar Symposium (IRS)*, 2022: IEEE, pp. 396-401.

[27] J. H. Ender and J. Klare, "System architectures and algorithms for radar imaging by MIMO-SAR," in *2009 IEEE Radar Conference*, 2009: IEEE, pp. 1-6.

[28] E. Fishler, A. Haimovich, R. Blum, D. Chizhik, L. Cimini, and R. Valenzuela, "MIMO radar: An idea whose time has come," in *Proceedings of the 2004 IEEE Radar Conference (IEEE Cat. No. 04CH37509)*, 2004: IEEE, pp. 71-78.

[29] C.-Y. Chen and P. P. Vaidyanathan, "MIMO radar space–time adaptive processing using prolate spheroidal wave functions," *IEEE Transactions on Signal Processing,* vol. 56, no. 2, pp. 623-635, 2008.

[30] F. Ahmad and R. M. Narayanan, "Conventional and emerging waveforms for detection and imaging of targets behind walls," in *Through-the-Wall Radar Imaging*: CRC Press, 2017, pp. 157-184.

[31] X. Fu, "Radar and Radar Imaging of Cooperative and Uncooperative Modulated Targets," 2019.

[32] B. Kang *et al.*, "All-optical and broadband microwave image-reject receiver based on phase modulation and I/Q balanced detection," *Journal of Lightwave Technology,* vol. 38, no. 21, pp. 5962-5972, 2020.

[33] K. J. Horadam, "Hadamard matrices and their applications," in *Hadamard Matrices and Their Applications*: Princeton university press, 2012.

[34] C. Knill, F. Embacher, B. Schweizer, S. Stephany, and C. Waldschmidt, "Coded OFDM waveforms for MIMO radars," *IEEE Transactions on Vehicular Technology,* vol. 70, no. 9, pp. 8769-8780, 2021.

[35] F. Guidi, N. Decarli, S. Bartoletti, A. Conti, and D. Dardari, "Detection of multiple tags based on impulsive backscattered signals," *IEEE Transactions on Communications,* vol. 62, no. 11, pp. 3918-3930, 2014.

[36] M. Zhang, Z. Zhou, M. Yang, Z. Liu, and Y. Yang, "A hybrid algorithm for the search of long binary sequences with low aperiodic autocorrelations," *Soft Computing,* vol. 25, no. 20, pp. 12725-12744, 2021.

[37] H. Rasouli, F. Rashidi, B. Karimi, and E. Khamehchi, "A surrogate integrated production modeling approach to long-term gas-lift allocation optimization," *Chemical Engineering Communications,* vol. 202, no. 5, pp. 647-654, 2015.

[38] Q. Gu, D. Wang, S. Jiang, N. Xiong, and Y. Jin, "An improved assisted evolutionary algorithm for data-driven mixed integer optimization based on Two_Arch," *Computers & Industrial Engineering,* vol. 159, p. 107463, 2021.

[39] L. F. Santos, C. B. Costa, J. A. Caballero, and M. A. Ravagnani, "Framework for embedding black-box simulation into mathematical programming via kriging surrogate model applied to natural gas liquefaction process optimization," *Applied Energy,* vol. 310, p. 118537, 2022.

[40] G. C. Onwubolu and M. Mutingi, "A genetic algorithm approach to cellular manufacturing systems," *Computers & industrial engineering,* vol. 39, no. 1-2, pp. 125-144, 2001.

[41] K. Takei, "Balanced orthogonal code for polarization angle diversity," in *2014 Asia-Pacific Microwave Conference*, 2014: IEEE, pp. 938-940.

[42] A. M. Molaei *et al.*, "Development of fast Fourier-compatible image reconstruction for 3D near-field bistatic microwave imaging with dynamic metasurface antennas," *IEEE Transactions on Vehicular Technology,* vol. 71, no. 12, pp. 13077-13090, 2022.

[43] A. M. Molaei, B. Zakeri, and S. M. H. Andargoli, "Passive localization and classification of mixed near-field and far-field sources based on high-order differencing algorithm," *Signal Processing,* vol. 157, pp. 119-130, 2019.

[44] S. A. Bawazeer, S. S. Baakeem, and A. A. Mohamad, "New approach for radial basis function based on partition of unity of Taylor series expansion with respect to shape parameter," *Algorithms,* vol. 14, no. 1, p. 1, 2020.

[45] S. Albeverio and R. Höegh-Krohn, "Oscillatory integrals and the method of stationary phase in infinitely many dimensions, with applications to the classical limit of quantum mechanics I," *Inventiones mathematicae,* vol. 40, no. 1, pp. 59-106, 1977.

[46] Y. Wu, L. J. Jiang, and W. C. Chew, "An efficient method for computing highly oscillatory physical optics integral," *Progress In Electromagnetics Research,* vol. 127, pp. 211-257, 2012.

[47] J. M. Lopez-Sanchez and J. Fortuny-Guasch, "3-D radar imaging using range migration techniques," *IEEE Transactions on antennas and propagation,* vol. 48, no. 5, pp. 728-737, 2000.

[48] X. Zhuge and A. G. Yarovoy, "Three-dimensional near-field MIMO array imaging using range migration techniques," *IEEE Transactions on Image Processing,* vol. 21, no. 6, pp. 3026-3033, 2012.

[49] L. Pulido-Mancera *et al.*, "Application of range migration algorithms to imaging with a dynamic metasurface antenna," *JOSA B,* vol. 33, no. 10, pp. 2082-2092, 2016.

[50] L. M. P. Mancera, "Analytical Modeling of Waveguide-fed Metasurfaces for Microwave Imaging and Beamforming," Duke University, 2018.

[51] M. E. Yanik and M. Torlak, "Near-field MIMO-SAR millimeter-wave imaging with sparsely sampled aperture data," *Ieee Access,* vol. 7, pp. 31801-31819, 2019.

[52] S. Jiacheng and M. Chen, "Research on Imaging Algorithm of Millimeter Wave Radar Based on Stolt Interpolation," in *2019 IEEE MTT-S International Microwave Biomedical Conference (IMBioC)*, 2019, vol. 1: IEEE, pp. 1-4.

[53] H. Gao *et al.*, "Study of the extended phase shift migration for three-dimensional MIMO-SAR imaging in terahertz band," *IEEE Access,* vol. 8, pp. 24773-24783, 2020.

[54] A. M. Molaei and A. Ebrahimzadeh, "Optimal steganography with blind detection based on Bayesian optimization algorithm," *Pattern Analysis and Applications,* vol. 22, pp. 205-219, 2019.

[55] G. Veerasamy, R. Kannan, R. Siddharthan, G. Muralidharan, V. Sivanandam, and R. Amirtharajan, "Integration of genetic algorithm tuned adaptive fading memory Kalman filter with model predictive controller for active fault-tolerant control of cement kiln under sensor faults with inaccurate noise covariance," *Mathematics and Computers in Simulation,* vol. 191, pp. 256-277, 2022.

[56] H. Hashemi, "The indoor radio propagation channel," *Proceedings of the IEEE,* vol. 81, no. 7, pp. 943-968, 1993.

[57] O. Yurduseven *et al.*, "Resolution of the frequency diverse metamaterial aperture imager," *Progress In Electromagnetics Research,* vol. 150, pp. 97-107, 2015.

[58] M. Zhou, Y. Alfadhl, and X. Chen, "Optimal spatial sampling criterion in a 2D THz holographic imaging system," *IEEE Access,* vol. 6, pp. 8173-8177, 2018.

[59] F. Sepehripour, A. S. Alavijeh, M. Fakharzadeh, and A. Khavasi, "A Broadband and Compact Millimeter-Wave Imaging System based on Synthetic Aperture Radar," *arXiv preprint arXiv:2205.14707,* 2022.

[60] Y. Meng, C. Lin, A. Qing, and N. K. Nikolova, "Accelerated Holographic Imaging With Range Stacking for Linear Frequency Modulation Radar," *IEEE Transactions on Microwave Theory and Techniques,* vol. 70, no. 3, pp. 1630-1638, 2021.

[61] S. Zhu and Z. Ding, "A simple approach of range-based positioning with low computational complexity," *IEEE Transactions on Wireless Communications,* vol. 8, no. 12, pp. 5832-5836, 2009.

[62] A. Liu *et al.*, "A survey on fundamental limits of integrated sensing and communication," *IEEE Communications Surveys & Tutorials,* vol. 24, no. 2, pp. 994-1034, 2022.

[63] U. Demirhan and A. Alkhateeb, "Integrated sensing and communication for 6G: Ten key machine learning roles," *arXiv preprint arXiv:2208.02157,* 2022.

[64] B. Gilvey and J. Trevelyan, "Numerical treatment of highly oscillatory PUBEM integrals," *Methods UKBIM12,* p. 25, 2019.

[65] M. Born and E. Wolf, *Principles of optics: electromagnetic theory of propagation, interference and diffraction of light*. Elsevier, 2013.

[66] X. Nie, C. Lin, and A. Qing, "FFT-SAR Algorithm for MIMO System Based on Stationary Phase Method," in *2020 IEEE Asia-Pacific Microwave Conference (APMC)*, 2020: IEEE, pp. 863-865.